Spectral and Chemical Characterization of Allophane and Imogolite

A Thesis

Presented in Partial Fulfillment of the Requirements for the

Degree of Master of Science

with a Major in Geology

in the

College of Graduate Studies

University of Idaho

by

Thomas J Jeute

Major Professor: Leslie L. Baker, Ph.D.

Committee Members: Daniel G. Strawn, Ph.D.; Thomas Williams, Ph.D.

Department Administrator: Leslie L. Baker, Ph.D.

August 2018

Authorization to Submit Thesis

This thesis of Thomas Jeute, submitted for the degree of Master of Science with a Major in Geology and titled "**Spectral and Chemical Characterization of Allophane and Imogolite,**" has been reviewed in final form. Permission, as indicated by the signatures and dates below, is now granted to submit final copies to the College of Graduate Studies for approval.

Major Professor: _____ Date: _____
                     Leslie L. Baker, Ph.D.

Committee Members: _____ Date: _____
                     Daniel G. Strawn, Ph.D.

                     _____ Date: _____
                     Thomas Williams, Ph.D.

Department Administrator: _____ Date: _____
                     Leslie L. Baker, Ph.D.

Abstract

Allophane and imogolite are nanophase hydrous aluminosilicate clay minerals. Their presence on Mars indicates a time when the presence of water was intermittent and likely short lived. Characterization of these materials has been difficult due to their amorphous characteristics and lack of long range crystallographic order. Fe-K Edge X-ray absorption spectroscopy, ^{29}Si and ^{27}Al Nuclear Magnetic resonance, Fourier transformed infrared spectroscopy, electron microscopy, and emission spectroscopy are used to gain insight on the spectral and chemical properties of these minerals. By using these combination of techniques a dichotomy of allophane species can be resolved, dependent upon Al:Si ratio. Additional insight is gained into the techniques that should be used, given a sample return mission from Mars.

Acknowledgements

I would like to thank my advisor, Dr. Leslie Baker, for the inspiration she provides to continue this type of research. Her positive attitude and scientific inquisitiveness was instrumental in the writing of this thesis.

I would also like to thank the NASA SSW program in funding this investigation, the Stanford Synchrotron Research Laboratory for the use of their synchrotron and for all of the research facilities at the University of Idaho that made this work possible.

Additional thanks are due to Dr. Alex Blumenfeld, whose NMR expertise helped us to gain some of the greatest insights contained within this report.

Dedication

This thesis is dedicated to the best rock hounding dog a geologist could ask for, thank you for

everything Lady Bug.

Table of Contents

List of Figures

List of Tables

1 Project Motivation

Mars has long been known to host fines on the surface. Findings in recent years have shown that a variety of poorly crystalline and fine-grained components are present in both at the surface. These highly variable amorphous and nanophase (np) materials likely represent partially altered basaltic or ash materials and identifying these on Mars will provide important clues about the aqueous geochemical environments.

The data presented here have helped to produce an understanding of the spectral, chemical, and x-ray signatures of imogolite, and primarily allophane. These new lab data will be compared with Martian data from sites likely to contain such phases to confirm their presence on Mars and to guide further synthesis of samples that best explain Martian outcrops. The results of this study benefit analyses of data from orbital CRISM and TES hyperspectral images, CheMin on curiosity, the mini Mössbauer instruments on the MER's and the APXS instruments on multiple rovers.

Additionally, this investigation has shed light on some of the primary techniques that should be used upon a sample return mission from Mars. Through the range of analyses performed, some proved to be more useful in certain regards than others. This information should be used to guide the handling of any samples that will be returned as well as to extract the largest amount of data possible to increase our understanding of Martian history.

Finally, this study will greatly improve our understanding of the geochemical conditions on Mars at sites where species such as opal, allophane, and imogolite exist and will significantly advance our knowledge of the aqueous geochemical environment(s) that have a bearing on whether conditions existed on Mars that could have supported life.

2 Background

2.1 Nanophase materials on Mars

Initial mineralogical mapping on Mars using thermal emission spectroscopy (TES) showed widespread regions of basaltic origin, and widespread regions of a more Si rich composition, above and below 30° latitude (Michalski et. al, 2005). These high Si regions, initially thought to be andesitic in composition, are latitude dependent. Upon reprocessing of some of the Mars Pathfinder lander data, these sites were found to contain signatures rich in H_2O(Foley et. al., 2003), suggesting an amorphous or smectite composition.

Continued analyses of Martian TES imagery (e.g. Christensen et al., 2001) produced a basic understanding of Martian geology, generalized by (1) global basaltic regions and (2) regions containing glass and alteration products (Wyatt and McSween, 2002; Morris et al., 2000; Bandfield et al., 2000; Rogers and Christensen, 2007). Gusev crater contains regions high in Si at Home Plate that likely include amorphous Si species such as opal or hydrated silica (Ruff et al. 2008; Morris et al., 2008; Squyres et al., 2008). Additional observations of amorphous Si were made using Compact Reconnaissance Imaging Spectrometer for Mars (CRISM) data (Murchie et al., 2009) at Valles Marineris (Milliken et al., 2008), Nili Fossae (Ehlmann et al., 2009) and Mawrth Vallis (Bishop et al., 2008). The Mars Exploration Rover's (MER's), Spirit and Opportunity, analyzed fine surficial material at Gusev (Spirit) and Meridiani (Opportunity) with the mini Mössbauer (Klingelhöfer et al., 2004; Morris et al., 2004, 2006a, b). Analyses indicated the presence of np ferric oxides, hydroxides, or oxyhydroxides (np-FeOx). This is consistent with previous visible/near-infrared (VNIR) detections of np-FeOx on Mars (Singer, 1982; Bell et al., 1990; Morris and Lauer, 1990).

An amorphous component was identified by the chemistry and mineralogy instrument (CheMin) on board the Mars Science Laboratory (MSL) rover at Gale Crater (Bish et al. 2013; Blake et al. 2013; Leshin et al., 2013) and could represent 20-30 wt.% of Martian surface material in many

locations. The amorphous component most likely represents a combination of amorphous glass and alteration products, composed primarily of Si, Fe, S and Al (Ming et al., 2014; Rampe et al., 2014; Vaniman et al., 2014; Morris et al., 2014). Rampe et al. (2012) identified 10-20% allophane and/or amorphous silica at North Acidalia, Solis Planum, Sinus Meridiani, and Aonium-Phrixi using TES imagery data. Bishop and Rampe (2012) found 10-20% allophane (or related phases) in phyllosilicate-rich outcrops at Mawrth Vallis using a combination of TES imagery and CRISM data. The elevated allophane detections in the northern plains (Rampe et al., 2012) could be related to observations of leached basaltic glass in this region (Horgan and Bell, 2012). Thus, allophane and imogolite could be a pervasive component of the Martian surface where water was present. Further, they may indicate periods of cyclical climate change. Progressive cooling and drying of the surface would result in conditions favorable for amorphous material production; where surface water was not present long enough to form more long-range order clays (Bishop and Rampe, 2016).

2.2   Allophane and imogolite morphology

Allophanes are poorly crystalline nanoscale aluminosilicates that are prevalent in soils formed from volcanic ash, and where an excess of Si and Al exist in solution (Parfitt, 1990; Childs et. al., 1990). They are frequently found in association with imogolite, most commonly as products of the weathering of volcanic tephras. Allophane imparts unique chemical and physical properties to soils in which it is a predominant mineralogical component, and those properties have implications for the content and retention of P and H_2O in such soils.

Allophane and imogolite exhibit rolled morphologies with nanometer-scale diameters, and therefore lack the long-range ordered orthogonal lattices observed in macroscopically crystalline materials, although imogolite exhibits long-range order in one direction. Although allophane and imogolite are difficult to characterize due to their small size and lack of macroscopic crystal ordering, research has illuminated much about their structure and formation.

Imogolite exhibits nanotubular morphology. Nanotubes are typically 6 nm in exterior diameter and the strands may be tens of nanometers in length. These tubes are thought to consist of a rolled gibbsite-like sheet of octahedrally coordinated Al with isolated silicon tetroxide tetrahedra bonded to the tube interior to yield an overall Al:Si ratio of 2:1 (Cradwick et. al., 1972). Each orthosilicate unit is bonded to three Al atoms and no silica polymerization is observed. Because of its tubular morphology, imogolite has no long-range structure in the cross-tube direction but does possess long-range structure in the along-tube direction. Computer modeling has confirmed this structure and reproduced the X-ray diffractogram of natural imogolite samples (Creton et. al., 2008a; Guimaraes et. al., 2007) In synthesis experiments, imogolite has been observed to evolve from nanospherical allophane-like structures upon aging for periods of >2 weeks (Levard et. al., 2010)

Due to the lack of long-range crystallographic order, allophanes have been difficult to characterize by standard methods such as X-ray diffraction (Parfitt, 2009), and most of the information known about their chemical structures has been determined by methods such as infrared spectroscopy, x-ray absorption spectroscopy (XAS), nuclear magnetic resonance (NMR), and by computer modeling.

Natural allophanes display a continuous variation in Al:Si ratio and a corresponding variation is observed in their structures. High-Al or proto-imogolite allophane exhibits an Al:Si ratio of approximately 2:1. It is thought to have a hollow, nanospherical structure that is similar in cross section to the cross-tube structure of imogolite. In the proposed structure, an exterior gibbsite-like sheet of octahedrally coordinated Al is rolled into a nanoball of diameter 3.5–6 nm. Orthosilicate units are bonded to the nanoball interior as in imogolite. Computer modeling suggests that four to six pores are present in the nanoball structure (Abidin et. al., 2007; Creton et. al., 2008b) These pores may permit exchange of ions or molecules into or out of the sphere likely affecting the

sorption properties of allophanes. Allophanes with higher Si contents have Al:Si ratios as low as 0.9 (Parfitt, 2009). NMR and Fourier transform infrared spectroscopy analyses suggest that high-Si allophanes formed in soil environments have a similar fundamental structure to high-Al allophanes, and that the additional silica is accommodated in a polymerized form in the nanoball interior (Parfitt, 1990). The lowest Al:Si ratios are found in "stream-deposit" allophanes that precipitate from silica-saturated stream or spring water (Wells et. al, 1977; Childs et. al. 1990; Parfitt, 1990). In these highly Si-enriched allophanes, the framework is proposed to be a nanospherical shell of polymerized Si, with a partial or fragmental octahedral Al (Al_O) shell and with some Al substitution in tetrahedral sites (Al_T) (Childs et. al., 1990). The tetrahedral Al substitution in these high Si species follows Lowenstein's rule for zeolites where no Al-O-Al linkages are allowed, resulting in a constant Al_T:Si of 1:3 (Childs et. al., 1990).

2.3 Allophane characterization

Fe-substituted natural and synthetic allophane and imogolite samples have been described (Kitagawa, 1973; Baker and Strawn, 2012). Several natural allophane samples were analyzed by Horikawa and Soezima (1977) using X-ray emission spectroscopy and they observed that Fe in these samples was distinct from Fe in Fe oxides, as well as from Fe in hisingerite and nontronite. Substitution of Fe into the structures of nano-aluminosilicates such as allophane has been reported to affect their morphology (Joussein et al., 2005), as well as the kinetics and end products of their ripening to more crystalline clay minerals (McBride et al., 1984; Farmer et al., 1991; Farmer, 1997). Iron-substituted allophanes may ripen to an Fe-depleted phase plus ferrihydrite (McBride et al., 1984), or they may recrystallize to Fe-bearing clays such as nontronite (Farmer et al., 1991) or ferruginous beidellite (Farmer, 1997). The specific conditions that lead Fe-bearing allophane to ripen into various end products are not well known.

Due to their lack of long-range crystal ordering, allophanes are difficult to study and their structure is still not completely understood, particularly with respect to the effect of widely varying Al:Si ratios in the same fundamental structural unit. The structure of imogolite, which has a more clearly defined Al:Si ratio, is better understood. The fundamental structural unit for both nano-aluminosilicates is thought to be an Al octahedral sheet (gibbsite sheet) rolled into a spheroidal, polyhedral, or tubular shape (Cradwick et al., 1972; Parfitt et al., 1980). In imogolite, Si is present as isolated tetrahedra bonded to the interior of the rolled gibbsite sheet by three Al-O-Si linkages, with one Si-OH pointing to the inside of the tube (Cradwick et al., 1972; Creton et al., 2008). In synthetic systems, small, curved sections with such a structure have been shown to form rapidly upon hydrolysis and to self-assemble upon heating to form nanotubes (Levard et al., 2010, 2011; Yucelen et al., 2011). Proto-imogolite allophane may have a similar structure to imogolite, but with the gibbsite sheet rolled into a spherical rather than tubular shape (Creton et. al, 2008a).

The location of additional Si in more Si-rich (feldspathoid type) allophanes is not well understood, although in very high-Si compositions the "skeleton" of the structure may be a rolled Si tetrahedral sheet with an incomplete Al octahedral sheet in its interior (Childs et al., 1990). An intermediate structure for Si-rich allophane based upon a curved kaolinite structure containing a defective tetrahedral sheet was proposed by Mackenzie et al. (1991). At present, no apparent consensus exists on whether high-Si and high-Al forms of allophane represent fundamentally different types of structure, or whether they represent a single fundamental structural type that is progressively modified to accommodate varying Al:Si ratios.

Infrared spectroscopic techniques have been a primary source of analytical data due to the ability to target individual bonds or bond characteristics. IR spectroscopy of allophane has produced an understanding of how Al:Si can influence band magnitudes in several wavenumber regions.

Parfitt et. al. (1980) showed that as Al:Si decreases, bands at 978 cm^{-1} and 348 cm^{-1} decrease in absorbance magnitude; while bands at 1020 cm^{-1} and 470 cm^{-1} increase in magnitude.

X-ray absorption fine structure spectroscopy (XAFS) is a useful technique for studying the structure of amorphous materials and nanominerals because it provides insight into short-range molecular structure at the atomic level, regardless of long-range structural order. The study of natural samples of poorly crystalline materials such as allophanes is complicated by variations in chemistry and by the possible presence of other mineral phases. To overcome this complexity, minerals synthesized in the laboratory under controlled conditions can be studied and compared to natural samples. In samples with Fe isomorphically substituted for Al, the Fe XAFS spectrum probes the short-range order in the octahedral sheet. The objective of the present study was to investigate Fe speciation and coordination state in synthetic and natural allophane and imogolite samples and to see how this structure changes with the addition of Fe and variation in Al:Si. The XAFS shell modeling was used to test existing models of allophane structure, and to examine the hypothesis that high-Al and high-Si forms of allophane have the same fundamental structure, based on a rolled octahedral sheet; and whether additional Fe incorporation modifies the results of these models.

3   Methods

3.1   Materials Synthesis

3.1.1   Allophane Synthesis

Using a method described by (Baker and Strawn, 2012) that was modified from Montarges-Pelletier (2005), a suite of synthetic allophane samples were created. This method was modified to produce varying amounts of Fe isomorphically substituted for Al in the allophanes by adding 0.1 M $FeCl_3$ to the starting solution. In this method, NaOH is titrated slowly into a mixture of 0.1 M $AlCl_3$ and $FeCl_3$ and tetraethyl orthosilicate (TEOS) under vigorous stirring to precipitate a gel. The gel is aged at 95 °C for five days (Figure 3.1). All syntheses were scaled to a total suspension volume of 1 L and the relative amounts of Fe and Al were modified volumetrically with the starting solution. The final supernatant from synthesis was decanted, preserved with a small amount of HNO_3, and saved for analysis. The precipitated gels were washed twice with deionized (DI) water, centrifuged for 15 min at 2400 RPM, and placed in dialysis tubing in DI water until the final conductivity was <5 μS cm^{-1}. The dialyzed gel was then frozen for storage, and then freeze dried for analysis.

Previously all work on synthetic allophanes had been done using Fe^{3+}, yet under Martian conditions, allophanes with Fe^{2+} may also be of significance. Accordingly, samples with Fe^{2+} isomorphically substituted were created. To inhibit oxidation of the Fe^{2+} during synthesis several precautions were taken. Deionized water was allowed to run through a polisher to ensure the water was completely deoxygenated. Solutions were combined in the same way as described above. To prevent oxidation during the synthesis, the experiment was performed under a N_2 purged atmosphere.

Some difficulties were encountered while incorporating Fe^{2+} into synthetic allophanes, because it was necessary to keep the sample completely away from contact with O2. The primary difficulty encountered was maintaining a consistent flow of N_2 into the experimental set up. As the

N_2 cylinder would deplete, pressures within the cylinder would lower and in turn the regulator would allow less flow though, given an equal setting. This was combatted by providing a higher flow rate, but the higher flow rate emptied the N_2 during the experiment and would allow the solution to oxidize. After several attempts the "Goldilocks" zone on the N_2 regulator was found and synthesis could resume.

Additional difficulties were encountered after synthesis, at the time of transferring and storing the samples while minimizing oxidation. Observations of the gel changing from blue to red, indicated that when exposed to the atmosphere, Fe in the gel samples would oxidize within several minutes time. Fe in freeze dried samples also oxidized by the end of the drying procedure. In order to prevent Fe oxidation, samples were stored frozen in gel form, and were analyzed in gel form at the synchrotron. Because of sample mounting limitations, it was not possible to analyze gel samples using any other instruments, so samples were freeze dried and in turn are oxidized for all other analyses.

Figure 3.1. Annotated picture of allophane synthesis set up. NaOH is titrated through tube in direction of green arrows. Red arrows indicate flow of nitrogen in Fe(II) syntheses.

3.1.2   2-Line Ferrihydrite Synthesis

2-line ferrihydrite was synthesized using the method described by Schwertmann et al. (2004). A solution of 0.1 M NaOH was titrated at a rate of 1 mL/min into a 50 mL aliquot of 0.1 M Fe(NO$_3$)$_3$ under constant stirring until the solution reached a pH of 7, using a total of 150 mL of NaOH altogether. The precipitate from this procedure was centrifuged and dialyzed in DI water. The gel was freeze- dried and was analyzed by X-ray diffraction (XRD) to confirm that the product was 2-line ferrihydrite.

3.1.3   Opaline silica Synthesis

A suite of opaline silica samples were synthesized using the Stöber process (Stöber et al., 1968), modified to include Fe. In this process, ammonium hydroxide is dissolved in ethanol and mixed with tetraethyl orthosilicate. The solution is stirred for several hours. Samples were prepared

with either a 0.1 M solution of $FeCl_3$ or a 0.1M solution of $Fe(NO_3)_3$ to achieve the desired final Fe

content.

3.1.4   Imogolite Synthesis

This process is included here for completeness, but we did not perform these imogolite

syntheses ourselves. A suite of synthetic imogolite samples were created by Z. Abidin using a

previously established method by Abidin et. al. 2014.   Aliquots of $AlCl_3$ solution were simultaneously

mixed with orthosilicic acid to yield an Al:Si ratio of 2:1. The solution mixtures were titrated with

NaOH at a rate of about 0.5 mL NaOH min^{-1} to an OH:Al molar ratio of 2. The Si concentration of the

resulting solution was 1.6 mM. Supernatant solutions had pH values from 3.98 to 4.03. The solution

mixtures were heated in an autoclave at 110°C for 48 hours. After the collected precipitates were

flocculated by NaCl, the sample was dialyzed using cellulose tubes against distilled water until they

were free of sodium and chloride ions, then freeze-dried.

3.2   Analysis Methods

3.2.1   Inductively Coupled Plasma Atomic Emission Spectroscopy

All supernatant solutions from synthesis experiments were analyzed on a ThermoFisher

iCAP Duo inductively-coupled plasma atomic emission spectrometer (ICP-AES) to verify synthesized

compositions. Samples were analyzed for Fe, Al and Si. Calibration solutions, a blank and a QC

solution were mixed using 0 PPM, 10 PPM and 50 PPM concentrations of proposed analytes with

small additions of HNO_3 and HCl to match preservation methods of supernatants. ICP results were

used to calculate the true anhydrous formula of the product, assuming the precipitant (allophane)

contains everything that wasn't left in the supernatant solution.

3.2.2   Fourier Transformed Infrared Spectroscopy

The FTIR analyses were carried out on a Perkin- Elmer System 2000 (Thermo Scientific,

Waltham, Massachusetts, USA), using a mixture of 3 wt.% sample in optical-grade KBr which was

lightly packed into a diffuse reflectance mounting geometry. Samples were scanned 100 times and

the spectra was then averaged. Spectra were recorded from 4000 to 600 cm^{-1} using 1 cm^{-1} resolution and processed using the Kubelka-Munk algorithm provided in Perkin Elmer Spectrum 2.0 software.

3.2.3 Field Emission Scanning Electron Microscopy

The SEM images were collected using a Zeiss Supra 35 field emission SEM (Carl Zeiss Microscopy GmbH, Jena, Germany) with a Noran System Six electron dispersive spectroscopic analyzer (EDS) (Thermo Scientific, Waltham, Massachusetts, USA). Samples were smeared onto carbon tape to prevent necessity of carbon coating. Micrographs were taken at magnifications ranging from 20,000x to 150,000x and analyzed at an accelerating voltage of 5kV. Semi-quantitative elemental analysis was carried out at 15kV using an EDS.

3.2.4 ^{27}Al and ^{29}Si Magic Angle Spin Nuclear Magnetic Resonance

Samples of Fe-substituted and Fe-free synthetic allophanes and imogolites were analyzed using ^{27}Al and ^{29}Si magic angle spinning (MAS) solid-state NMR on a Bruker Avance 500 MHz spectrometer (Bruker Biospin, Rheinstetten, Germany). Samples were spun at 12.6 kHz and were allowed to run until a signal to noise ratio of greater than 500 was achieved. Samples with high Fe^{3+} contents were not run due to their paramagnetic nature.

3.2.5 Powder X-Ray Diffraction

X-ray diffraction analyses were ran using a Siemens Diffraktometer D5000. Samples were prepared as a lightly packed powder to ensure random orientation. This machine uses CuKα radiation generated at 40kV and 30mA. The samples were measured from 2° to 80° 2θ with a step size of 0.05° 2θ and a measuring time of 4 seconds per step.

3.2.6 X-Ray Absorption Spectroscopy

Bulk Fe K- edge XANES and EXAFS analyses were performed at beamline 7-3 of the Stanford Synchrotron Radiation Laboratory (SSRL). Beamline 7-3 is fed by the SPEAR ring operating with a beam current of 500-495 mA. The x-rays are diverted using a 20 pole 2-tesla wiggler source then

through a vertical collimating mirror into the monochromator. The monochromator for this

beamline is two parallel Si(220) crystals with a 6-mm entrance slit. This experimental setup results in

a spot size of approximately 3 x 15 mm. A LYTLE detector was used to collect fluorescence

measurements over the entire EXAFS energy range of 6880-7873 eV with an energy step size of

0.35eV. All spectra were collected at 10 K using a liquid He cryostat and scanned 4-12 times to

prevent beam damage and to increase the signal to noise ratio. These multiple scans were then

calibrated to an Fe foil and merged using the program Athena (Ravel and Newville, 2005).

Allophane samples were packed into aluminum sample holders of 0.7-mm thick and held in

place with Kapton tape. High-Fe imogolite, ferrihydrite, and nontronite samples were smeared in a

thin layer on filter paper, which was cut into strips, stacked three layers thick, and sealed in the

sample holder with Kapton tape.

3.2.7   FEFF Modeling
The merged spectra were normalized and background subtracted using a cubic spline.

Fitting of the spectra was done in R-space (Fourier transformed chi spectra) in the program Artemis

(Ravel and Newville, 2005) using theoretical paths modified after Creton (2008a). The fitting strategy

used in this study follows the approach described by and Baker and Strawn (2012) and Baker et. al

(2014) in previous studies of Fe in clay minerals.

Shell fitting of the allophane samples was carried out using the 6-shell allophane nanoball

model as well as a 6-shell dioctahedral smectite model, following the modelling philosophy of Baker

and Strawn (2014). Atomic coordinates for the smectite model were taken from Tsipursky and Drits

(1984) and coordinates for the nanoball model were taken from a section of the model nanoball

described by Creton et al. (2008a). Paths were generated from the atomic coordinates using the

program Atoms (Ravel, 2001) and shell fitting was carried out using the program Artemis (Ravel and

Newville, 2005). In fitting, all path lengths were optimized at first, and were then constrained to be

equal within fit. Fe-O3 shell distances were fixed for all models except the 1:2 Fe(III), where allowing it to float resulted in a better fit. Debye-Waller XAFS factors were optimized for the first Fe-O1 shell and fixed to be equal to the former for the Fe-Fe, Fe-Al, and Fe-Si backscattering paths. Debye-Waller XAFS factors were also optimized for the Fe-O2 and then fixed to be equal for the Fe-O3 shell. Octahedral sites were fitted with either Fe or Al, with the total number of Fe-Metal backscatterers constrained to sum to three, resulting in a dioctahedral sheet. Trioctahedral fits, where Fe-Metal backscatters sums to 6, were attempted for the Fe(II) substituted samples, but no recognizable improvement in the fit was observed. The path length was optimized for the Fe-Si backscattering path, with the number of Si atoms fixed at 2 for the smectite model and 3 for the nanoball model.

In the atomic structure proposed by Creton et. al (2008a), the nanoball is constructed of a rolled octahedral sheet with unpolymerized Si coordinated to the interior or exterior of the sphere. Each Si atom is coordinated to three Al atoms via Al-O-Si bonds, and the fourth O (O3 in the present paper) atom points towards the center of the sphere. The most significant difference between a conventional smectite structure and the theoretical allophane structure is the distance of the Si atom; three Si atoms are present at a modeled $r_{effective}$ distance of 3.14-3.16 Å, rather than the four Si atoms at 3.18 to 3.24 Å found in 2:1 phyllosilicates (Baker and Strawn, 2012)(Table 3.1). In addition, because there is no tetrahedral sheet polymerization in the proto-imogolite model, no tetrahedral O (O2) atoms are present. Resulting in the second backscattering O shell in this structure consisting of six octahedral O (Oi) atoms corresponding to the O atoms in the adjacent octahedra, and three backscattering O atoms (O3) at 3.98 Å from the central Fe atom (the hydroxyl on the Si-OH apices pointing toward the interior of the nanosphere). Additional differences between the structures occur at greater distances but were not taken into account in these models.

Nanoball			Smectite		
Path	**CN**	**R**	**Path**	**CN**	**R**
Fe-O1	6.00	1.920	**Fe-O1**	6.00	1.898
Fe-Fe	NFe	2.992	**Fe-Fe**	NFe	3.149
Fe-Al	3-NFe	2.992	**Fe-Al**	3-NFe	3.149
Fe-Si	3.00	3.150	**Fe-Si**	2.00	3.217
Fe-Oi	6.00	3.511	**Fe-O2**	1.00	3.445
Fe-O3	3.00	3.984	**Fe-O3**	6.00	3.702

Table 3.1. Table showing starting parameters for both the nanoball and smectite models. R is in angstroms and represents the starting values in the EXAFS modelling.

4 Results

4.1 Compositions Achieved

4.1.1 Synthetic Allophane

The sample compositions span the range of naturally occurring allophanes from high Si (molar Al:Si 1:2) to protoimogolite (molar Al:Si 2:1); a middle member of molar Al:Si 1:1 was also created. These three Al:Si compositions were then synthesized with molar 0%, 2%, 5%, and 10% Fe^{3+} isomorphically substituted for Al. This yielded 12 samples of allophane with varying compositions and physical properties.

Due to the reducing environment present on Mars, synthetic allophanes with Fe^{2+} may also be of significance. Substitution of Fe^{2+} should be more difficult due to the relative size difference with Al as well as the charge difference. Al^{3+} has an atomic radius of 0.5 while Fe^{3+} has a radius of 0.64 and Fe^{2+} has a radius of 0.76. With Si^{4+} having an atomic radius of 0.41, Fe^{2+} should be relatively incompatible within the allophane structure.

Figure 4.1. Picture of Fe-free and Fe(III)-substituted allophane samples.

Several difficulties in the experiment were encountered while synthesis of the Fe^{2+} substituted allophanes was carried out (see Methods). Due to multiple failed attempts of a composition of 1:1 Al:Si, and the completion of both endmembers; only samples of high Si (molar Al:Si 1:2) and protoimogolite (molar Al:Si 2:1) were created having 10% Fe^{2+} content.

Previous synthetic work suggested that the amount of Fe that can substitute in synthetic allophane varies with Si content (Baker et al., 2014). Current synthetic work suggests otherwise, in that we have achieved 10 mol.% Fe isomorphically substituted for Al in allophanes with Al:Si compositions up to 2:1.

4.1.2   Synthetic Opaline Silica

Varying compositions of Fe-free and Fe-substituted opaline silica samples were created using the previously established methodology. Syntheses using both $FeCl_3$ and $Fe(NO_3)_3$ were performed to investigate possible differences in the precipitant compositions.

4.2   Analysis Results

4.2.1   Fourier Transform Infrared Spectroscopy

Several characteristic differences can be observed in the Kubelka-Munk transformed FTIR spectra. Increases in Si content in the allophane structure results in more intense bands at 1200-900 cm^{-1} as well as 3750-2700 cm^{-1}. Smaller increases in absorbance magnitude in the 3750-2700 cm^{-1} range can also be observed with the addition of Fe^{3+} into the structure, while the addition of Fe^{2+} seems to have the opposite effect.

Figure 4.3 illustrates the differences in the various compositions of allophane. The three main absorption bands indicative of an allophane like structure can be seen in both the Fe^{2+}, Fe^{3+} bearing and non-Fe bearing species. With the addition of Si into the structure, absorption magnitude increases. Additionally, the 1200-800 cm^{-1} absorption band begins to develop shoulders at approximately 1150 and 950 cm^{-1}. When Fe^{3+} and Fe^{2+} are introduced to the structure, the

absorbance magnitude is also amplified; with Fe^{3+} substitutions resulting in greater amplification.

The magnitude amplification of both the silicate and hydroxyl regions is less evident in the

allophanes with an Al:Si ratio of 1:1. This results in allophanes with a composition of low Si (Al:Si 2:1)

and high Fe (3-6%+) to show a greater absorbance magnitude in both the hydroxyl and silicate

regions, than its 1:1 counterpart (Figure 4.3, I and H).
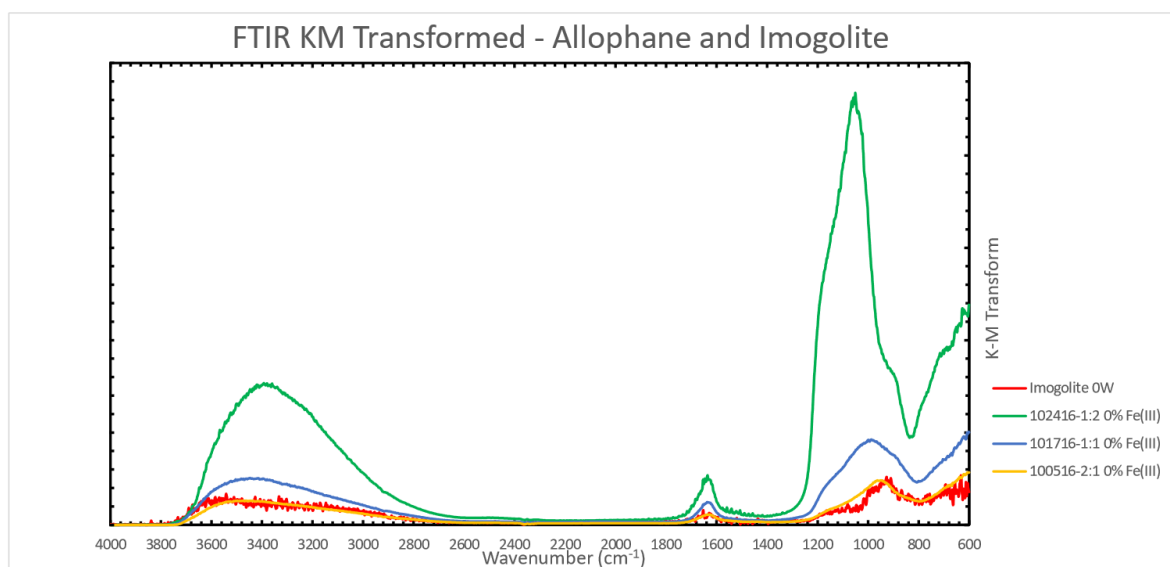
Figure 4.2. Fe-Free allophanes spectra. Kubelka-munk transformed reflectance measurements for allophanes in this study
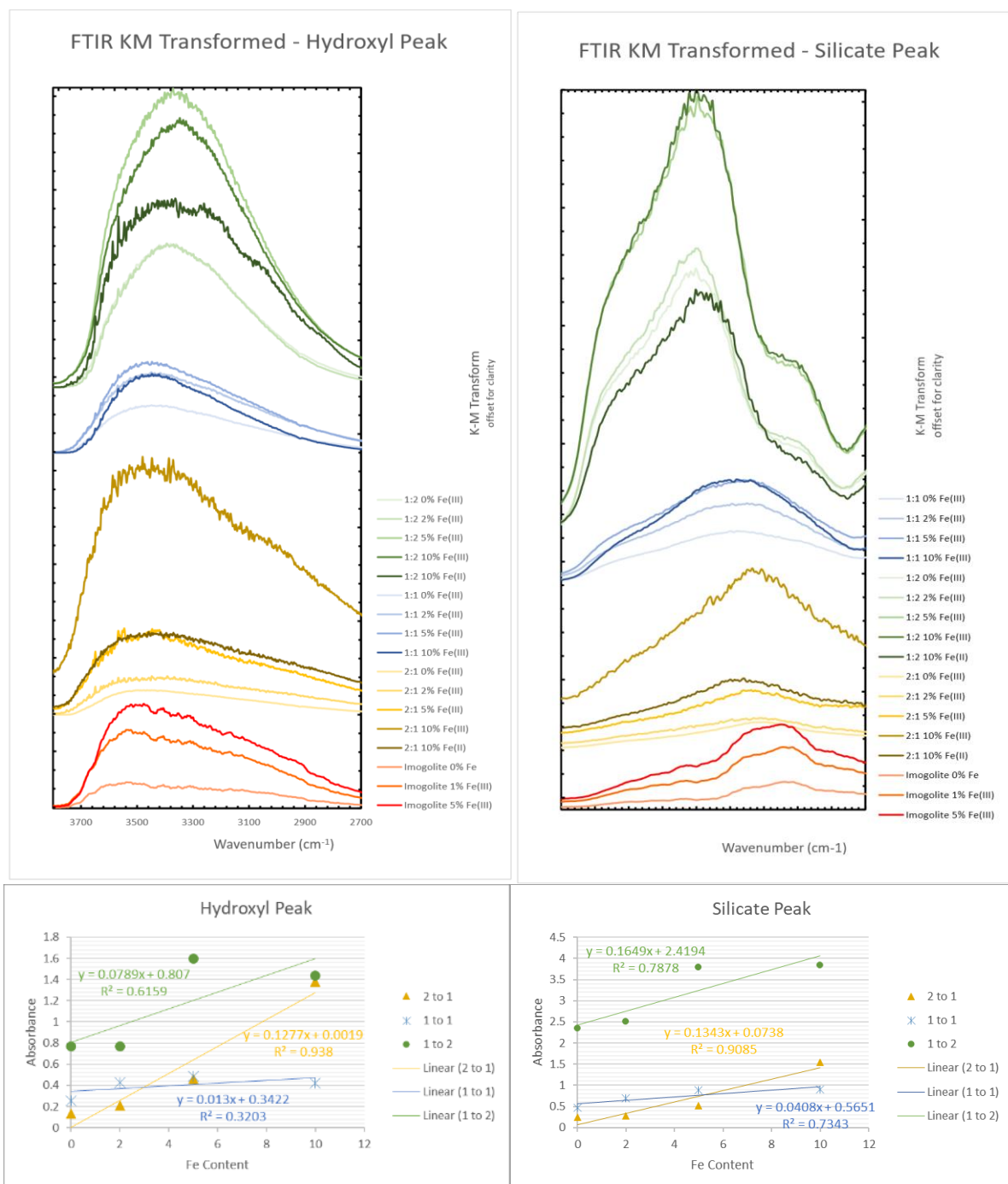
Figure 4.3. Kubelka-munk transformed reflectance measurements for allophanes in this study **TOP LEFT:** Kubelka-munk transformed reflectance data for the hydroxyl region (3800-2700 cm^{-1}) of the spectra. **TOP RIGHT:** Kubelka-munk transformed reflectance data for the silicate region (1250-800 cm^{-1}) of the spectra. **BOTTOM LEFT:** Scatter plot showing the relation between both Al:Si ratio and Fe content in magnitude of the hydroxyl peak region. **BOTTOM RIGHT:** Scatter plot showing the relation between both Al:Si ratio and Fe content in magnitude of the silicate peak region.

4.2.2 Inductively Coupled Plasma Atomic Emission Spectroscopy

Results from the ICP-AES for Fe, Al, and Si were used to calculate the true Al:Si ratio, the

true Fe content and to show possible incompatibilities at endmember species. Results for Fe^{3+} and

non-Fe bearing species are displayed in Table 4.1. Synthesis parameters align well with the

calculated results. Downward trends in calculated Al:Si correlate with increases in Fe content. Figure

4.4 shows the relationship with linear fits displayed. The downward trend in Al:Si ratio is more

pronounced with greater amounts of Al in the structure.

Allophane Samples	Synthesis Parameters		Calculated Results	
	Al:Si	Fe (III) molar %	Al:SI	Fe %
100516-2:1	2.00	0.00%	2.016	0.00%
121916-2:1	2.00	2.00%	1.970	2.04%
011917-2:1	2.00	5.00%	1.916	5.26%
013117-2:1	2.00	10.00%	1.820	11.09%
101716-1:1	1.00	0.00%	1.018	0.00%
103116-1:1	1.00	2.00%	1.025	2.03%
110716-1:1	1.00	5.00%	1.010	5.24%
111416-1:1	1.00	10.00%	0.948	11.11%
121116-1:2	0.50	2.00%	0.515	2.04%
112816-1:2	0.50	5.00%	0.502	5.26%
120416-1:2	0.50	10.00%	0.478	11.11%

Table 4.1. Table showing select allophane samples with their synthesis parameters and the actual results calculated from the ICP-AES data.
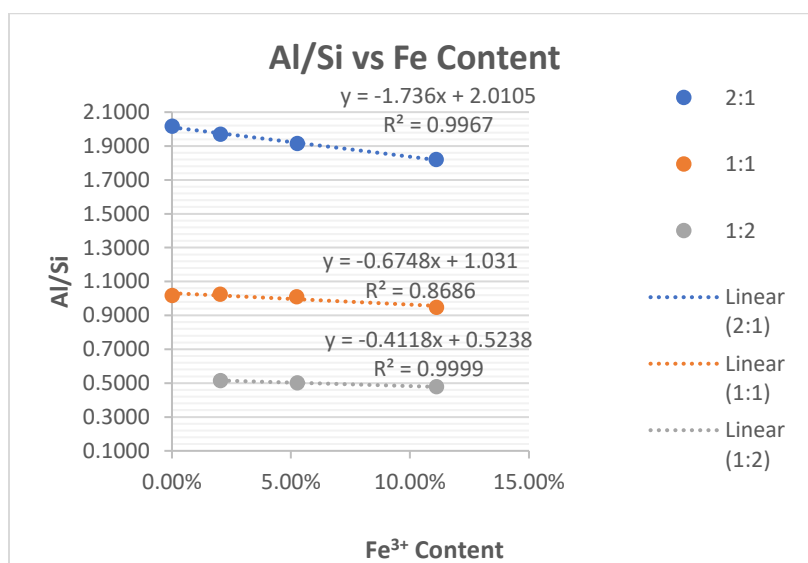
Figure 4.4 Graph showing select allophane samples with their calculated Fe content plotted against the calculated Al:Si ratio.

4.2.3 ^{27}Al MAS Nuclear Magnetic Resonance

^{27}Al Magic angle spinning nuclear magnetic resonance results for Fe^{2+} and non-Fe bearing

allophane compositions are displayed in Figure 4.5. Relative abundances of four-coordinated (Al_T),

five-coordinated (Al_P) and six-coordinated Al (Al_O) in the allophane structure can be quantified by

integration of the peak curves. The peaks are located at ~10, ~36, and ~60 ppm for Al_O, Al_P, and Al_T,

respectively. Two distinct peaks predominate and can be seen correlating with four and six

coordinated Al. Samples with increased Si content tend towards increased tetrahedrally coordinated

Al in the structure. Furthermore, the addition of Fe^{2+} into the allophane structure results in

increased Al_T as well.
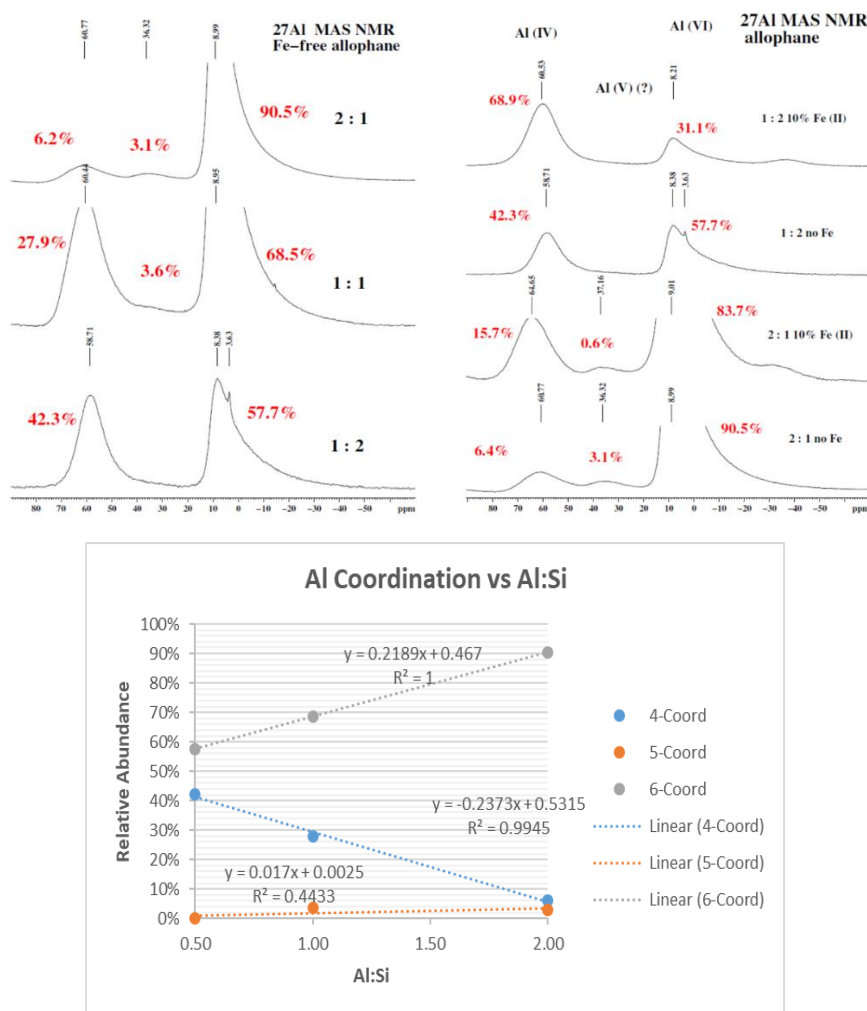
Figure 4.5. ^{27}Al MAS NMR data of Fe-free and Fe(II) substituted allophane samples. The relation between Al:Si ratio and Al coordination can be observed more clearly in the accompanying graph.

4.2.4 ^{29}Si MAS Nuclear Magnetic Resonance

^{29}Si magic angle spinning nuclear magnetic resonance results for Fe^{2+} and non-Fe bearing allophane compositions are displayed below (Figure 4.6). Unlike the large shifts seen in the Al NMR data, which correlate to Al coordination number; Small shifts seen in the peak differentiation in the Si NMR data are strongly correlated to Si polymerization. The small shifts seen in Si NMR data are also useful for evaluating the number of Al 'neighbors' in the structure. This data can be used to study the Al/Si ordering in the allophane structure. Allophanes with a 2:1 Al:Si exhibit a spectrum with a fairly well resolved peak at ~79 ppm. As Si is introduced into the structure a poorly resolved, broad peak signature develops centered at ~100 ppm in the 1:2 Al:Si samples. The 1:1 Al:Si samples exhibit both features with the well resolved peak at ~78 ppm having similar magnitude to the less well resolved feature at ~100 ppm.
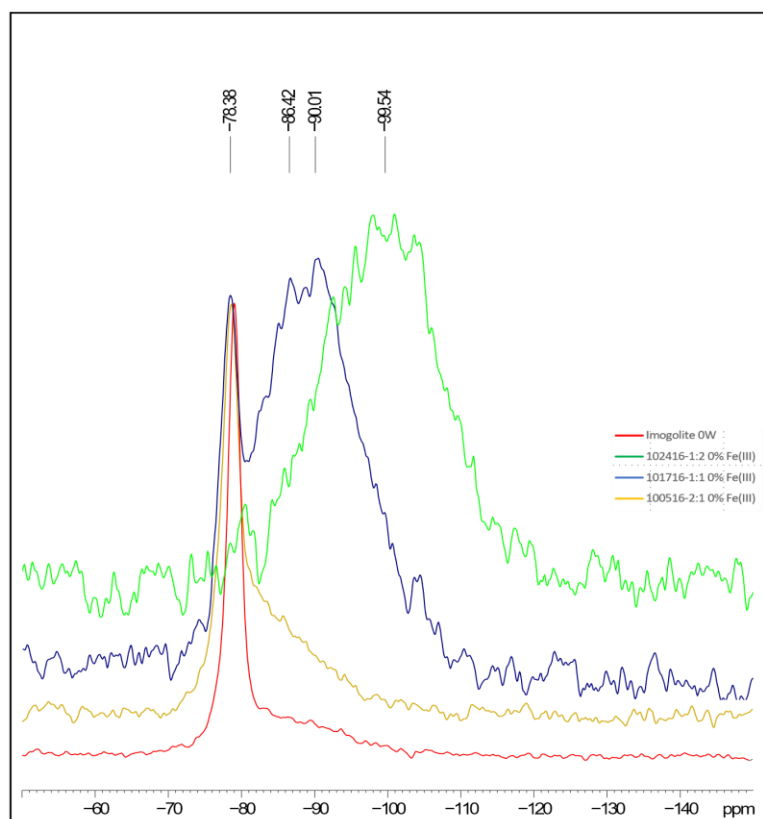
Figure 4.6. ^{29}Si NMR data for three selected Fe-free allophanes. The two endmember species, 2:1 and 1:2 illustrate markedly different characteristics in how Si is polymerized, while the 1:1 shows a mix between the two.

4.2.5   Field Emission Scanning Electron Microscopy

Several electron micrographs of a 1:2 Al:Si allophane sample were captured.

Nanospherical colloids comprise the majority of what was captured, yet the nanosphere

morphology is distinct (Figure 4.7).
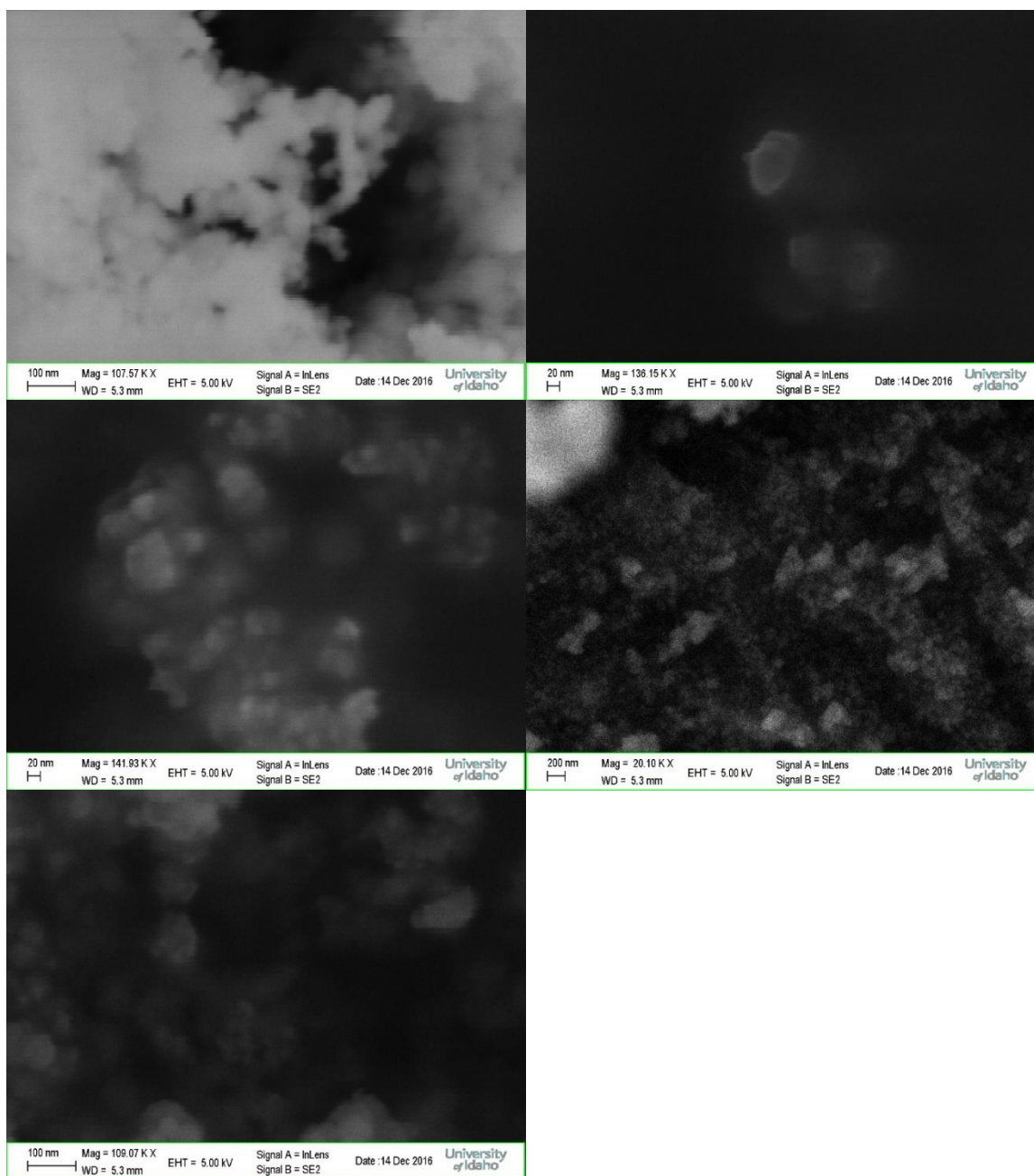
Figure 4.7. FESEM images of selected allophane samples. Allophane colloids can be observed in all images

4.2.6   Powder XRD

XRD data do not show systematic changes in the allophane structure with either Al:Si or

Fe content. In all samples, broad peaks are present at ~12° and ~26° 2θ. Slight changes in the

asymmetry of the 12° peak can be seen in the high Al samples with the addition of Fe, but this

relation is not present in the high Si samples. Both the 0% Fe 2:1 composition and the 1:1

composition display small broad peaks at ~40° 2θ. This feature is not present in the 10% Fe 2:1

sample (Figure 4.8).
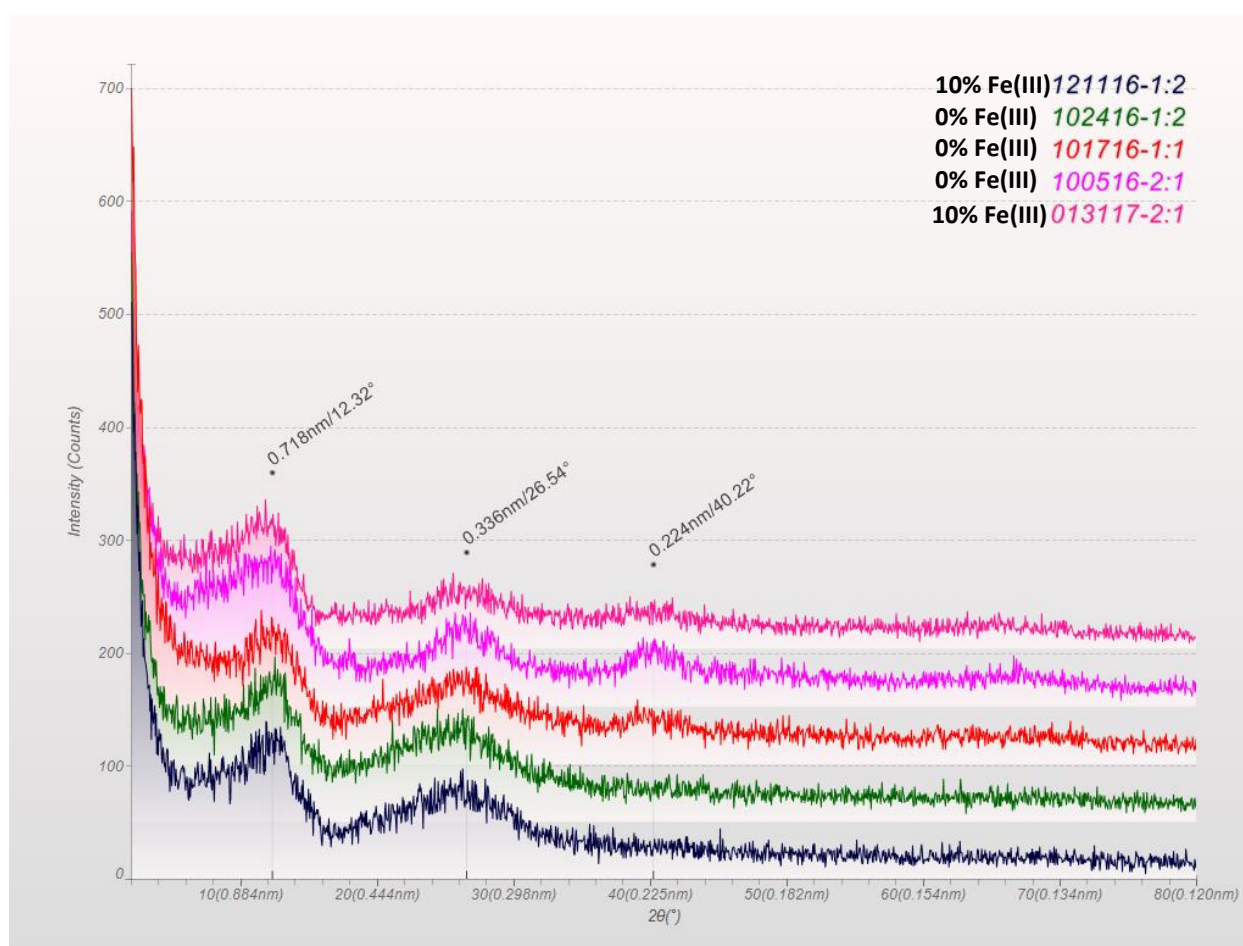
Figure 4.8. X-ray diffraction data for selected allophanes from 2° to 80° 2θ. Diffuse peaks at 12.32, 26.54, and 40.22 are labeled above.

4.2.7   XANES

XANES spectra of the Fe substituted allophanes is displayed in Figure 4.9. Slight shifts to

lower energy in edge inflection position are can be seen in the two Fe(II) substituted samples. Edge

positions for Fe(III) samples are near 7128eV and near 7124eV for Fe(II) samples. Changes in pre-edge character can also be seen to correlate with Al:Si (Figure 4.10). Splitting of the pre-edge region occurs with the addition of Si in both the Fe(III) and Fe(II) substituted samples. This pre-edge split in the 1:1 ratio is smaller in magnitude than the high Si sample. The high Al sample has no discernible split in the pre-edge region.
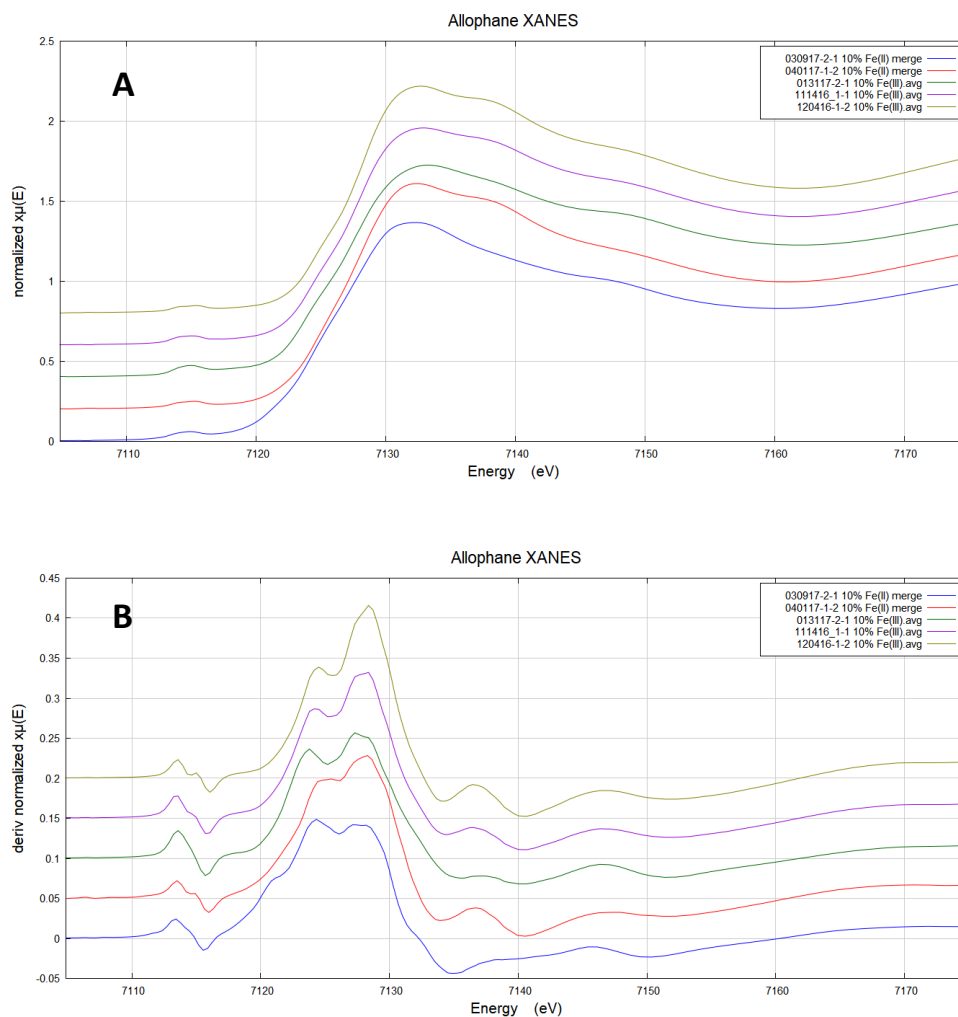
Figure 4.9. XANES spectra of 10% Fe(III) (1:2 gold, 1:1 purple, 2:1 green) and 10% Fe(II) (1:2 red, 2:1 blue). **A:** XANES edge features offset for clarity and plotted in terms of energy. Changes in the pre-edge signature are discernible and shifts to lower energy in the edge inflection point are visible. **B:** 1st derivative of XANES spectra of the same region as **A.** Changes in pre-edge character and edge location are visible.
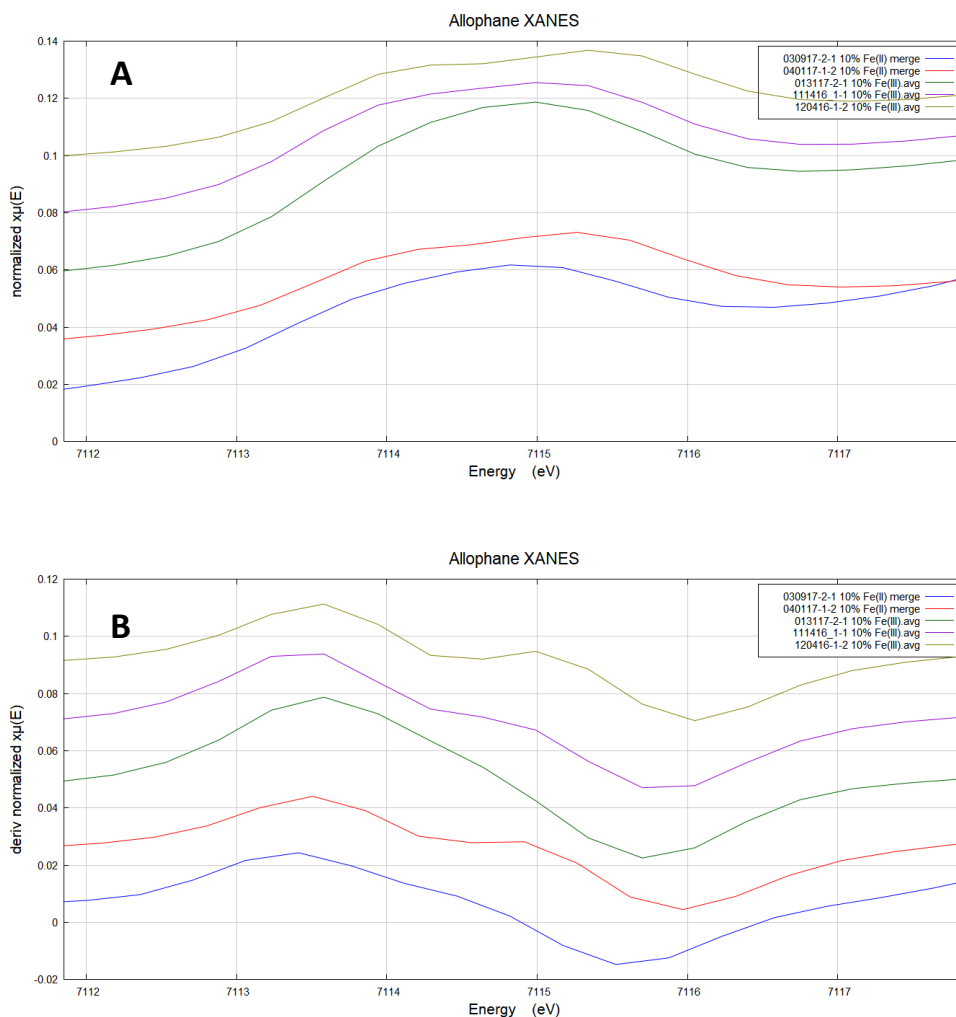
Figure 4.10. XANES pre-edge spectra of 10% Fe(III) (1:2 gold, 1:1 purple, 2:1 green) and 10% Fe(II) (1:2 red, 2:1 blue). **A:** XANES pre-edge spectra illustrating splitting in pre-edge feature with the addition of Si into the structure. **B:** 1st derivative of XANES pre-edge spectra illustrates the splitting in the pre-edge, present in both Fe(III) and Fe(II) substituted samples.

4.2.8 EXAFS-Nanoball Model

Coordination numbers, path lengths, and Debye-Waller factors for Fe^{3+} substituted samples

are displayed in Table 4.2 and Table 4.3. Fe-Fe coordination numbers for Fe substituted samples are

highest with high Al content, 1.96 for Fe(III) and 1.50 for Fe(II) and decrease with the addition of Si

to ~1.65 for Fe(III) and 0.58 for Fe(II). Fe-O1 path lengths exhibit very similar values for all samples,

ranging from 1.97 to 1.99. The shortest Fe-O1 path lengths correlate with the highest Al, Fe(III)

sample. Fe-Fe path lengths are consistent between 3.00 to 3.06 Å. Fe-Al path lengths are typically

slightly shorter than Fe-Fe path lengths and range from 2.99 to 3.04 Å. Fe-Si path lengths cluster

between 3.24 and 3.28 Å.

Differences become much more pronounced when looking at the Fe-Oi path lengths. All the

samples have Fe-O2 path lengths that are consistently lower than those of Baker and Strawn (2012);

ranging from 3.68 to 3.79 Å. For Fe(III) substituted samples, path lengths decrease slightly with the

addition of Si; the opposite relation is seen for Fe(II) samples. The Fe-O3 path was fixed for all

models at 3.98.

4.2.9   EXAFS-Smectite Model

Model fits, coordination numbers, path lengths, and Debye-Waller factors for Fe^{3+}

substituted samples are displayed in Figure 4.11, Table 4.2, and Table 4.3. Fe-Fe coordination

numbers for Fe substituted samples are higher in all cases than the nanoball model. Fe-O1 path

lengths exhibit very similar values for all samples, ranging from 1.97 to 2.00. The shortest Fe-O1

path lengths, again, correlate with the highest Al Fe(III) sample. Interestingly, when Fe(II) is

substituted, this composition resulted in the longest Fe-O1 bond length. Fe-Fe path lengths are

consistent between 3.03 to 3.08 Å. Fe-Al pathlengths are typically slightly shorter than Fe-Fe path

lengths and range from 3.01 to 3.06 Å. Fe-Si path lengths cluster between 3.23 and 3.28 Å.

Similar to the nanoball model, differences in modeled path lengths become much larger

when looking at the Fe-O2 path lengths. All the samples have Fe-O2 path lengths that are

consistently lower than Baker and Strawn (2012) and range from 3.34 to 3.51 Å. For all samples

except the high 1:1 Fe(III) sample, Fe-O3 path lengths were fixed at 3.70. For the 1:1 composition,

the Fe-O3 path length was allowed to float, resulting in a path length of 3.78Å. The 1:1 composition

converged on much shorter path lengths of 3.03 for Fe-O2 when Fe-O3 was fixed at 3.70.

Figure 4.11. EXAFS Modeled and real spectra of the modeled allophane samples. Arranged by Al:Si descending and by model type and composition left to right.

Path	Nanoball Model														
	1to2 10%Fe			1to1 10%Fe			2to1 10%Fe			2to1 10%Fe (II)			1to2 10%Fe (II)		
	eO	-3.043		eO	-3.787		eO	-4.111		eO	-1.554		eO	-4.776	
	R factor	0.004		R factor	0.011		R factor	0.007		R factor	0.011		R factor	0.011	
	CN	R	σ^2	CN	R	σ^2	CN	R	σ^2	CN	R	σ^2	CN	R	σ^2
Fe-O1	6.00	1.99	0.006	6.00	1.99	0.006	6.00	1.97	0.008	6.00	1.99	0.009	6.00	1.99	0.007
Fe-Fe	1.96	3.06	0.006	1.63	3.03	0.006	1.67	3.00	0.008	1.50	3.06	0.009	0.58	3.01	0.007
Fe-Al	1.04	3.04	0.006	1.37	3.01	0.006	1.33	2.99	0.008	1.50	3.01	0.009	2.42	3.02	0.007
Fe-Si	3.00	3.28	0.006	3.00	3.28	0.006	3.00	3.24	0.008	3.00	3.26	0.009	3.00	3.27	0.007
Fe-Oi	6.00	3.79	0.030	6.00	3.76	0.023	6.00	3.75	0.022	6.00	3.68	0.040	6.00	3.72	0.019
Fe-O3	3.00	3.98	0.030	3.00	3.98	0.023	3.00	3.98	0.022	3.00	3.98	0.040	3.00	3.98	0.019

Path	Smectite Model														
	1to2 10%Fe-S			1to1 10%Fe-S			2to1 10%Fe-S			2to1 10%Fe (II)-S			1to2 10%Fe (II)-S		
	eO	-2.325		eO	-2.498		eO	-3.255		eO	0.364		eO	-3.968	
	R factor	0.005		R factor	0.006		R factor	0.008		R factor	0.012		R factor	0.011	
	CN	R	σ^2	CN	R	σ^2	CN	R	σ^2	CN	R	σ^2	CN	R	σ^2
Fe-O1	6.00	1.99	0.006	6.00	1.99	0.006	6.00	1.97	0.008	6.00	2.00	0.010	6.00	1.99	0.007
Fe-Fe	2.01	3.05	0.006	2.22	3.06	0.006	2.10	3.03	0.008	2.22	3.08	0.010	0.95	3.03	0.007
Fe-Al	0.99	3.01	0.006	0.78	3.06	0.006	0.90	3.04	0.008	0.78	3.02	0.010	2.05	3.02	0.007
Fe-Si	2.00	3.28	0.006	2.00	3.26	0.006	2.00	3.23	0.008	2.00	3.23	0.010	2.00	3.28	0.007
Fe-O2	1.00	3.51	0.052	1.00	3.50	0.018	1.00	3.34	0.029	1.00	3.38	0.028	1.00	3.39	0.029
Fe-O3	6.00	3.70	0.052	6.00	3.79	0.018	6.00	3.70	0.029	6.00	3.70	0.028	6.00	3.70	0.029

Table 4.2. Table with coordination numbers (CN), radial distances in angstroms (R), and Debye -Waller factors in angstroms squared (σ^2) for allophane samples with 10% Fe composition. R factor is a measure of the quality of the model fit, lower R factor means a better fit. (For model outputs see Appendix).

10% Fe Substituted Allophanes

	Fe-O1	Fe-Fe	Fe-Al	Fe-Si	Fe-O2	Fe-O3
1to2 10%Fe	1.99	3.06	3.04	3.28	3.79	3.98
1to1 10%Fe	1.99	3.03	3.01	3.28	3.76	3.98
2to1 10%Fe	1.97	3.00	2.99	3.24	3.75	3.98
2to1 10%Fe (II)	1.99	3.06	3.01	3.26	3.68	3.98
1to2 10%Fe (II)	1.99	3.01	3.02	3.27	3.72	3.98
1to2 10%Fe-S	1.99	3.05	3.01	3.28	3.51	3.70
1to1 10%Fe-S	1.99	3.06	3.06	3.26	3.50	3.79
2to1 10%Fe-S	1.97	3.03	3.04	3.23	3.34	3.70
2to1 10%Fe (II)-S	2.00	3.08	3.02	3.23	3.38	3.70
1to2 10%Fe (II)-S	1.99	3.03	3.02	3.28	3.39	3.70
2to1 Baker	1.99	3.04	2.98	3.25	3.78	3.93
1to1 Baker	1.99	3.08	2.97	3.24	3.79	3.92
1to3Baker	1.99	3.11	2.97	3.20	3.78	4.00

Table 4.3. Line chart and accompanying data illustrate trends in modeled radial distances(Å) from the absorber Fe atom in 10% Fe substituted allophane samples. Data associated with the nanoball modeling structure are colored in shades of blue and smectite modelling structure results are colored in shades of gray and denoted with a "-S" at the end of their sample name. (For model outputs see Appendix).

5   Discussion

5.1   FTIR

Results from the FTIR spectroscopy illustrate different characteristics for the varying compositions of allophanes that were created. The primary changes in the spectra occur in the hydroxyl stretching region (3800-2700 cm^{-1}) and in the Si bending region (1250-800 cm^{-1}). In both endmember species, a distinct positive correlation between the magnitude of these absorption bands and the Fe(III) content is present. When Fe(II) is substituted instead of Fe(III) the absorbance magnitude is still elevated above an Fe-free sample but to a lesser degree that of the same Fe(III) content. The 1:1 allophane samples however, display a much less obvious, if existent at all, positive correlation between Fe(III) content and absorbance magnitude.

When Fe content is held constant and Al:Si is varied, the largest differences in band development occur. Absorbance magnitude in the hydroxyl region increases with the addition of Si into the structure. Absorbance magnitude in the Si polymerization region also increases with the addition of Si. Si polymerization band peaks for the 2:1 and 1:1 composition allophanes are centered at ~965 cm^{-1} and shifts to 1040 cm^{-1} for the 1:2 composition, causing a shoulder to develop at 965 cm^{-1}.

5.2   ICP-AES

Results from the emission spectroscopy show a strong correlation between intended sample composition and actual composition, indicating a successful synthesis. Additionally, when calculated Al:Si and calculated Fe % are plotted with each other patterns can be recognized (Figure 4.4). True isomorphic substitution should result in a slope equivalent to that of the Al:Si ratio. These results show that allophanes with a 2:1 Al:Si resulted in a slope of 1.74, 1:1 allophanes with a 1:1 Al:Si resulted in a slope of 0.67, and 1:2 Al:Si allophanes resulted in a slope of 0.41. The 1:1

composition has the most divergence from the theoretical value of 1 and contains the lowest R^2

value.

	Al_T/Al_O from NMR Data	Al_T:Si	Al:SI	Fe %
100516-2:1	6.63%	13%	2.02	0.00%
121916-2:1	10.74%	21%	1.97	2.04%
101716-1:1	28.99%	29%	1.02	0.00%
103116-1:1	24.04%	25%	1.02	2.03%
102416-1:2	42.37%	21%	0.50	0.00%
121116-1:2	57.14%	29%	0.52	2.04%
112816-1:2	55.25%	28%	0.50	5.26%

Table 5.1. Table of the selected allophane samples that have both NMR data and ICP calculated formulas.

For samples where [27] Al NMR data and ICP-AES data were both available, a positive

correlation between Si content and Al_T content can be resolved. When the NMR data is used in

conjunction with the ICP data, a trend emerges. The Al_T:Si ratio stays rather consistent at ~1:3,

consistent with high Si allophanes at Silica Springs in Childs et. al. (1990) (Table 5.1). This ratio also

follows Loewenstein's rule for zeolites. Loewenstien's rule for zeolites states that no Al-O-Al linkages

are allowed within the tetrahedral sheet due to charge imbalances (Loewenstein, 1954). This

represents a tetrahedral Si sheet with Al_T tetrahedra substituted in, with no Al_T tetrahedra sharing

edges.

5.3   ^{29}Si NMR

The ^{29}Si NMR data show two distinct peak morphologies indicating an ordered Si structure at

high Al contents (proto-imogolites) and a less ordered structure at high Si contents, consistent with

Parfitt (1990) and Childs et. al. (1990). These data are consistent with two distinct morphologies of

allophanes, dependent upon the Al:Si ratio. Allophanes with high Si content are likely structured

around a main tetrahedral Si and Al sheet skeleton, with incomplete octahedral sheets attached to

the interior and/or exterior. Allophanes with high Al contents have an octahedral skeleton with

incomplete tetrahedral Si and Al sheets attached to the interior and/or exterior. High degrees of Si

polymerization in a variety of bond configurations results in the broad peak seen in high Si allophane NMR data.

5.4 ^{27}Al NMR

^{27}Al NMR data illustrates the relative abundances of tetrahedral (Al_T), pentahedral (Al_P), and octahedral (Al_O)in the selected allophane samples. With the addition of Si into the structure, an increased abundance of Al_T is observed. This increase in Al_T is likely related to an increase in the polymerization or 'filling in' of the tetrahedral sheet. As this tetrahedral sheet grows, increased Al will be taken up preferentially to the tetrahedral sheet before going into the octahedral sheet. When Fe is introduced to the structure, more Al_T is present as well. This indicates a stronger affinity for Fe in the octahedral sheet, as Al is preferentially placed into the tetrahedral sheet. Al_P abundances stay relatively consistent in the varying compositions; these are most likely representative of low degrees of Al octahedral disorder at the pore edge boundaries of the proposed nanoball model.

5.5   Powder XRD

Powder XRD results do not show any systematic changes in spectra as a result of Al:Si or of Fe content. The presence of a small broad peak at approximately 40° 2θ at low Fe concentrations, and the absence at high concentrations could possibly show changes in the structure. Due to the broad and diffuse nature of this peak, quantitative measurements are unlikely.

5.6   EXAFS Modeling

Modelling of the Fe substituted allophanes aligns well with Baker and Strawn (2014) in the Fe-O1, Fe-Fe, Fe-Al, and Fe-Si bond path lengths. The Fe-O1 shell at ~1.99 is consistent with Fe in octahedral coordination. Fe-Fe backscattering distances in the nanoball model show a negative correlation with the addition of Si into the structure, but this correlation is not present in the smectite modeled structure. Additionally, differences smaller than 0.02 angstrom are typically

unresolvable in EXAFS data (Ravel and Newville, 2005). In all cases, Fe-Al backscattering paths were slightly shorter than Fe-Fe backscattering paths, likely due to the increased atomic radius of Fe as compared to Al.

One of the primary differences in the nanoball and smectite structures at this scale is the Fe-Si backscattering distance. In the nanoball structure, Fe-Si distances should be closer to 3.14. Modeled results show a range of distances from 3.23 to 3.28, much closer to the smectite structure of 3.18 to 3.24 modeled by Baker and Strawn (2014). An allophane model with polyhedral structure that had slightly curved faces rather than a sphere was proposed by Creton et al. (2008). If allophane has such a polyhedral structure, that may explain why the interatomic distances for the Fe-Si backscatterers observed in the present study align with those in flat octahedral sheets.

Similar to the Fe-Si distance, the Fe-Oi/O2 distance can be one of the primary indicators between the nanoball and smectite structural models. Octahedral sheet path lengths, Fe-O1, Fe-Fe, Fe-Al, and Fe-O3 are modeled as similar path lengths in both structures due to the rigidity of the octahedral sheet; while the Fe-Si and Fe-Oi/O2 are path lengths connected to the tetrahedral sheet, where the largest structural changes at this scale occur. Fe-Oi/O2 distances vary the greatest within this study, ranging from 3.68 to 3.79 Å for the nanoball model and range from 3.34 to 3.51 Å. These distances span the range of modeled distances between the smectite model (3.44 Å) and the nanoball model (3.51). Due to the low signal contribution from O at this distance, conclusions can be murky, but several interesting relations emerge.

In the nanoball model, Fe-Oi path lengths decrease slightly with the addition of Al into the structure, from 3.79 to 3.75Å. The shortest Fe-Si path length coincides with the shortest Fe-Oi path length, leading to the conclusion that increased Al content would hold the tetrahedral sheet at a

slightly closer proximity. This could be due to increased ordering within the Al octahedral sheet creating a more rigid framework skeleton to attach Si tetrahedra to.

For the smectite sample, Fe-O2 path lengths decrease with the addition of Al into the structure as well. Again, the shortest path length for both the Fe-Si and Fe-O2 coincides with the high Al sample. A common recurrence during the fitting of these samples in the smectite model was recorded. During fits, the Fe-O2 shell would very easily be pushed to a distance greater than the Fe-O3 shell. This was remedied by changing the initial seed value for ΔR of the Fe-O2 to either 0.1 or -0.1. This procedure could not remedy these results for the 1:1 Fe(III) sample and so the Fe-O3 path length was allowed to float. This difficulty is likely due to the mixed nature of the allophane sample at this intermediate composition. This resulted in path lengths of 3.50 and 3.79Å for the Fe-O2 and Fe-O3 shells, respectively.

6   Conclusions

Several findings have been made throughout the scope of this project. Previous synthetic work suggested that the amount of Fe that can be substituted into the allophane structure varies with Al:Si. This work suggested that high Al samples could only accept up to approximately 2 mol % Fe. Current syntheses have succeeded in compositions of 10 mol.% Fe(III) and Fe(II) substituted into the high Al endmember. The substitution and structural position was confirmed using XANES.

FTIR spectra indicate changes in the OH and Si structural parameters. Changes in the OH region likely indicate changes in the amount of water included in the allophane structure, while changes in Si polymerization information are held in the Si region of the spectra. Future work, including Loss on Ignition, and P sorption isotherms will help quantitatively describe this.

NMR spectra show some of the largest differences in the allophane compositions. ^{29}Si NMR data show distinct differences between the two endmember allophane compositions. The 1:1 ratio, displays a mix of both signature. This observation correlates with the idea that allophane can either be composed of a complete tetrahedral sheet with an incomplete octahedral sheet at high Si content; or can be composed of a complete octahedral sheet with an incomplete tetrahedral sheet at high Al content. This would explain why the 1:1 allophane seems to show a mix of these two characters, it likely is a mix of the two endmember types of allophane. Changes in nanoball radii might be detectable under SEM if this is true.

Slight changes in Fe-Oi/O2 path lengths correlate with Al:Si content. The shortest path occurs in the 2:1 samples and could be indicative of a closer tetrahedral sheet at these compositions. The decrease in Fe-Oi/O2 correlates with a decrease in the Fe-Si in both modelling cases, which could also correlate to a closer tetrahedral sheet.

Observations during EXAFS modelling included an increased difficulty in achieving a good fit with the smectite model. Path lengths would quickly converge to nonsensical values if not constrained. Due to the ease of the nanoball fits, these models seem more likely to the author.

One of the goals of this project was to provide background on analytical methods that could be used when a sample return mission from Mars is achieved. The greatest increases in knowledge of these nanophase materials throughout this project was done using NMR. With the combination of chemical constraints, this data could be used in distinguishing mineral phases and possible environments of deposition. (e.g. Al rich allophanes are typically soil components while Si rich allophanes are indicative of stream deposits)

Fe K-edge X ray absorption spectroscopy was quite useful as well. While, distinguishing allophane compositions with XAS might be unlikely, the ability to distinguish mineral species from each other is invaluable with the high likelihood of mixed amorphous phases in Martian samples.

References

Abidin Z., Matsue N. & Henmi T. (2007) Differential formation of allophane and imogolite: Experimental and molecular orbital study. Journal of Computer-Aided Materials Design, 14, 5-18.

Abidin Z., Matsue N. & Henmi T. (2009) Validity of the New Method for Imogolite Synthesis and Its Genetic Implication. Interdisciplinary Studies on Environmental Chemistry – Environmental research in Asia, 331-341.

Abidin Z., Matsue N. & Henmi T. (2014) A new method for synthesis of imogolite. Patent registered in Japan: http://jstore.jst.go.jp/nationalPatentDetail.html?pat_id=22303.

Baker, L.L. and Strawn, D.G. (2012) Fe K-edge XAFS spectra of phyllosilicates of varying crystallinity. Physics and Chemistry of Minerals, 39,675-684.

Baker, L.L. and Strawn, D.G. (2014) XAFS study of Fe-substituted allophane and imogolite. Clays and Clay Minerals, 62, 20-34.

Bandfield J.L., Christensen P.R. & Smith M.D. (2000) Spectral dataset factor analysis and endmember recovery: Application to analysis of Martian atmospheric particulates. Journal of Geophysical Research, 105, 9573-9587.

Bell J.F., III, McCord T.B. & Owensby P.D. (1990) Observational evidence of crystalline iron oxides on Mars. Journal of Geophysical Research, 95, 14,447-14,461.

Bish D.L., Blake D.F., Vaniman D.T., Chipera S.J., Morris R.V., Ming D.W., Treiman A.H., Sarrazin P., Morrison S.M., Downs R.T., Achilles C.N., Yen A.S., Bristow T.F., Crisp J.A., Morookian J.M., Farmer J.D., Rampe E.B., Stolper E.M., Spanovich N. & Team M.S. (2013) X-ray diffraction results from Mars Science Laboratory: Mineralogy of Rocknest at Gale Crater. Science, 341, doi: 10.1126/science.123893.

Bishop J.L. & Rampe E.B. (2012) Allophane identified at Mawrth Valles in CRISM and TES datasets and implications for the ancient phyllosilicate-rich rocks. 43rd Lunar Planet Sci. Conf., abs. #2277.

Bishop J.L. & Rampe E.B. (2016) Evidence for a changing Martian climate from the mineralogy at Mawrth Vallis. Earth and Planetary Science Letters,448, 42-28.

Bishop J.L., Noe Dobrea E.Z., McKeown N.K., Parente M., Ehlmann B.L., Michalski J.R., Milliken R.E., Poulet F., Swayze G.A., Mustard J.F., Murchie S.L. & Bibring J.-., P. (2008) Phyllosilicate diversity and past aqueous activity revealed at Mawrth Vallis, Mars. Science, 321, doi: 10.1126/science.1159699, pp. 830-833.

Blake D.F., Morris R.V., Kocurek G., Morrison S.M., Downs R.T., Bish D., Ming D.W., Edgett K.S., Rubin D., Goetz W., Madsen M.B., Sullivan R., Gellert R., Campbell I., Treiman A.H., McLennan S.M., Yen A.S., Grotzinger J., Vaniman D.T., Chipera S.J., Achilles C.N., Rampe E.B., Sumner D., Meslin P.-Y., Maurice S., Forni O., Gasnault O., Fisk M., Schmidt M., Mahaffy P., Leshin L.A., Glavin D., Steele A., Freissinet C., Navarro- González R., Yingst R.A., Kah L.C., Bridges N., Lewis K.W., Bristow T.F., Farmer J.D., Crisp J.A., Stolper E.M., Des

Marais D.J., Sarrazin P. & Team M.S. (2013) Curiosity at Gale Crater, Mars: Characterization and analysis of the Rocknest sand shadow. Science, 341, doi:10.1126/science.1239505.

Childs, C.W., Parfitt, R.L., and Newman, R.H.(1990) Structural studies of Silica Springs allophane. Clay Minerals 25, 329-341.

Christensen, P.R., 26 colleagues, 2001. Mars Global Surveyor Thermal Emission Spectrometer experiment: investigation description and surface science results. Journal of Geophysical Research. 106 (E10), 23823–23871.

Cradwick, P.D.G., Farmer, V.C., Russell, J.D., Masson, C.R., Wada, K., and Yoshinaga, N. (1972) Imogolite, a hydrated aluminum silicate of tubular structure. Nature Physical Science, 240,187-189.

Creton, B., Bougeard, D., Smirnov, K.S., Guilment, J., and Poncelet, O.G. (2008a) Structural model and computer modeling study of allophane. Journal of Physical Chemistry C, 112, 358-364.

Creton, B., Bougeard, D., Smirnov, K.S., Guilment, J., and Poncelet, O. (2008b) Molecular dynamics study of hydrated imogolite. 1. Vibrational dynamics of the nanotube. The Journal of Physical Chemistry C, 112, 10013-10020.

Ehlmann B.L., Mustard J.F., Swayze G.A., Clark R.N., Bishop J.L., Poulet F., Marais D.J.D., Roach L.H., Milliken R.E., Wray J.J., Barnouin-Jha O. & Murchie S.L. (2009) Identification of hydrated silicate minerals on Mars using MRO-CRISM: Geologic context near Nili Fossae and implications for aqueous alteration. Journal of Geophysical Research, 114, doi:10.1029/2009JE003339.

Farmer, V.C. (1997) Conversion of ferruginous allophanes to ferruginous beidellites at 95º under alkaline conditions with alternating oxidation and reduction. Clays and Clay Minerals, 45,591-597.

Farmer, V.C., Krishnamurti, G., and Huang, P. (1991) Synthetic allophane and layer-silicate formation in SiO2- Al2O3-FeO-Fe2O3-MgO-H2O systems at 23ºC and 89ºC in a calcareous environment. Clays and Clay Minerals, 39, 561-570.

Foley, C.N., Economou, T.E., Clayton, R.N., 2003. Calibration of the Mars pathfinder alpha proton X-ray spectrometer. Journal of Geophysical Research. 108 (E12).

Guimarares L., Enyashin, A.N., Frenzel, T., Duarte, H.A., and Seifert, G. (2007) Imogolite Nanotubes: Stability, Electronic, and Mechanical Properties. ACS Nano, 1, 4, 362-368.

Horgan B. & Bell J.F. (2012) Widespread weathered glass on the surface of Mars. Geology, doi: 10.1130/G32755.1.

Horikawa, Y. and Soezima, H. (1977) State analysis of iron in allophanic clays II: Iron L-emission band spectra from allophanic clays and hisingerite by the use of an X-ray microanalyzer. Clay Science, 5,97-102.

Joussein, E., Petit, S., Churchman, J., Theng, B., Righi, D., and Delvaux, B. (2005) Halloysite clay minerals – a review. Clay Minerals, 40,383-426.

Kitagawa, Y. (1973) Substitution of aluminum by iron in allophane. Clay Science, 4,151-154.

Klingelhöfer G., Morris R.V., Bernhardt B., Schröder C., Rodionov D., de Souza P.A.J., Yen A.S., Gellert R., Evlanov E.N., Zubkov B., Foh J., Bonnes U., Kankeleit E., Gütlich P., Ming D.W., Renz F., Wdowiak T.J., Squyres S.W. & Arvidson R.E. (2004) Jarosite and hematite at Meridiani Planum from Opportunity's Mössbauer spectrometer. Science, 306, 1740-1745.

Leshin L.A., Mahaffy P.R., Webster C.R., Cabane M., Coll P., Conrad P.G., Archer P.D., Atreya S.K., Brunner A.E., Buch A., Eigenbrode J.L., Flesch G.J., Franz H.B., Freissinet C., Glavin D.P., McAdam A.C., Miller K.E., Ming D.W., Morris R.V., Navarro-González R., Niles P.B., Owen T., Pepin R.O., Squyres S., Steele A., Stern J.C., Summons R.E., Sumner D.Y., Sutter B., Szopa C., Teinturier S., Trainer M.G., Wray J.J., Grotzinger J.P. & Team M.S. (2013) Volatile, isotope, and organic analysis of Martian fines with the Mars Curiosity rover. Science, 341, doi: 10.1126/science.1238937.

Levard C., Rose J., Thill A., Masion A., Doelsch E., Maillet P., Spalla O., Olivi L., Cognigni A., Ziarelli F. & Bottero J.Y. (2010) Formation and growth mechanisms of imogolite-like aluminogermanate nanotubes. Chemistry of Materials, 22, 2466-2473.

Loewenstein, W. (1954) The distribution of aluminum in the tetrahedra of silicates and aluminates American Mineralogist, 39, 92-96.

MacKenzie, K., Bowden, M., and Meinhold, R. (1991) The structure and thermal transformations of allophanes studied by 29Si and 27Al high resolution solid-state NMR. Clays and Clay Minerals, 39,337-346.

Manceau, A., Chateigner, D., and Gates,W.P. (1998) Polarized EXAFS, distance-valence least-squares modeling (DVLS), and quantitative texture analysis approaches to the structural refinement of Garfield nontronite. Physics and Chemistry of Minerals, 25,347-365.

McBride, M.B., Farmer, V.C., Russell, J.D., Tait, J.M., and Goodman, B.A. (1984) Iron substitution in aluminosilicate sols synthesized at low pH. Clay Minerals, 19,1-8.

Michalski, J.R., Kraft, M.D., Sharp, T.G., Williams, L.B., Christensen, P.R., 2005. Mineralogical constraints on the high-silica martian surface component observed by TES. Icarus. 174, 161-177.

Milliken R.E., Swayze G.A., Arvidson R.E., Bishop J.L., Clark R.N., Ehlmann B.L., Green R.O., Grotzinger J., Morris R.V., Murchie S.L., Mustard J.F. & Weitz C.M. (2008) Opaline silica in young deposits on Mars. Geology, 36, 847-850; doi: 10.1130/G24967A.1.

Ming D.W., Archer P.D., Glavin D.P., Eigenbrode J.L., Franz H.B., Sutter B., Brunner A.E., Stern J.C., Freissinet C., McAdam A.C., Mahaffy P.R., Cabane M., Coll P., Campbell J.L., Atreya S.K., Niles P.B., Bell J.F., Bish D.L., Brinckerhoff W.B., Buch A., Conrad P.G., Des Marais D.J., Ehlmann B.L., Fairén A.G., Farley K., Flesch G.J., Francois P., Gellert R., Grant J.A., Grotzinger J.P., Gupta S., Herkenhoff K.E., Hurowitz J.A., Leshin L.A., Lewis K.W., McLennan S.M., Miller K.E., Moersch J., Morris R.V., Navarro- González R., Pavlov A.A., Perrett G.M., Pradler I., Squyres S.W., Summons R.E., Steele A., Stolper E.M., Sumner D.Y., Szopa C., Teinturier S., Trainer M.G., Treiman A.H., Vaniman D.T., Vasavada A.R., Webster C.R., Wray

J.J., Yingst R.A. & Team M.S. (2014) Volatile and Organic Compositions of Sedimentary Rocks in Yellowknife Bay, Gale Crater, Mars. Science, 343, doi: 10.1126/science.1245267.

Montarges-Pelletier, E., Bogenez, S., Pelletier, M., Razafitianamaharavo, A., Ghanbaja, J., Lartiges, B., and Michot, L. (2005) Synthetic allophane-like particles: textural properties. Colloids and Surfaces A: Physicochemical and Engineering Aspects, 255,1-10.

Morris R.V. & Lauer Jr. H.V. (1990) Matrix effects for reflectivity spectra of dispersed nanophase (superparamagnetic) hematite with application to Martian spectral data. Journal of Geophysical Research, 95, 5101-5109.

Morris R.V., Graff T., Lane M.D., Golden D.C., Schwandt C.S., Shelfer T.D., Ming D.W., Mertzman S.A., Bell III J.F., Crisp J.A. & Christensen P.R. (2000) Acid sulfate alteration products of a tholeiitic basalt: Implications for interpretation of martian thermal emission spectra. Lunar Planet Science Conf., Abstr. #2014.

Morris R.V., Klingelhöfer G., Bernhardt B., Schröder C., Rodionov D.S., de Souza P.A., Jr., Yen A.S., Gellert R., Evlanov E.N., Foh J., Kankeleit E., Güttlich P., Ming D.W., Renz F., Wdowiak T.J., Squyres S.W. & Arvidson R.E. (2004) Mineralogy at Gusev Crater from the Mössbauer Spectrometer on the Spirit Rover. Science, 305, 833-836.

Morris R.V., Klingelhöfer G., Schröder C., Rodionov D.S., Yen A., Ming D.W., de Souza P.A.J., Wdowiak T., Fleischer I., Gellert R., Bernhardt B., Bonnes U., Cohen B.A., Evlanov E.N., Foh J., Gütlich P., Kankeleit E., McCoy T., Mittlefehldt D.W., Renz F., Schmidt M.E., Zubkov B., Squyres S.W. & Arvidson R.E. (2006b) Mössbauer mineralogy of rock, soil, and dust at Meridiani Planum, Mars: Opportunity's journey across sulfate-rich outcrop, basaltic sand and dust, and hematite lag deposits. Journal of Geophysical Research, 111, doi:10.1029/2006JE002791.

Morris R.V., Klingelhöfer G., Schröder C., Rodionov D.S., Yen A.S., Ming D.W., de Souza P.A.J., Fleischer I., Wdowiak T.J., Gellert R., Bernhardt B., Evlanov E.N., Zubkov B., Foh J., Bonnes U., Kankeleit E., Gütlich P., Renz F., Squyres S.W. & Arvidson R.E. (2006a) Mössbauer mineralogy of rock, soil, and dust at Gusev crater, Mars: Spirit's journey through weakly altered olivine basalt on the plains and pervasively altered basalt in the Columbia Hills. Journal of Geophysical Research, 111, doi: 10.1029/2005JE002584.

Morris R.V., Ming D.W., Gellert R., Vaniman D.T., Bish D.L. & etal. (2014) Chemical composition of crystalline, smectite, and amorphous components for Rocknest Soil and John Klein and Cumberland Mudstone drill fines using APXS, CheMin, and SAM datasets from Gale Crater, Mars. Lunar Planet Science Conf., Abstr. #1319.

Morris R.V., Ming D.W., Gellert R., Yen A., Clark B.C., Graff T.G., Arvidson R.E. & Squyres S. (2008) The hydrothermal system at Home Plate in Gusev Crater, Mars: Formation of high silica material by acid-sulfate alteration of basalt. Lunar Planet Sicence Conf., Abstr. #2208.

Murchie S.L., Mustard J.F., Ehlmann B.L., Milliken R.E., Bishop J.L., McKeown N.K., Noe Dobrea E.Z., Seelos F.P., Buczkowski D.L., Wiseman S.M., Arvidson R.E., Wray J.J., Swayze G.A., Clark R.N., Des Marais D.J., McEwen A.S. & Bibring J.P. (2009) A synthesis of Martian aqueous

mineralogy after 1 Mars year of observations from the Mars Reconnaissance Orbiter. Journal of Geophysical Research, 114, doi: 10.1029/2009JE003342.

Parfitt R.L. (1990) Allophane in New Zealand--a review. Australian Journal of Soil Research, 28, 343-360.

Parfitt, R.L. (2009) Allophane and imogolite: role in soil biogeochemical processes. Clay Minerals, 44,135-155.

Parfitt, R.L. and Henmi, T. (1980) Structure of some allophanes from New Zealand. Clays and Clay Minerals, 28,285-294.

Rampe E.B., Kraft M.D., Sharp T.G., Golden D.C., Ming D.W. & Christensen P.R. (2012) Allophane detection on Mars with Thermal Emission Spectrometer data and implications for regional-scale chemical weathering processes. Geology, 40, doi:10.1130/G33215.1.

Rampe E.B., R. V. Morris, S. W. Ruff, B. Horgan, E. Dehouck, C. N. Achilles, D. W. Ming, D. L. Bish, S. J. Chipera, and MSL Science Team (2014) Amorphous Phases on the Surface of Mars, 8th International Conf. on Mars, Pasadena, Abstr. #1239.

Ravel B. & Newville M. (2005) ATHENA, ARTEMIS, HEPHAESTUS: data analysis for X-ray absorption spectroscopy using IFEFFIT. Journal of Synchrotron Radiation, 12, 537-541.

Ravel, B. (2001) ATOMS: crystallography for the X-ray absorption spectroscopist. Journal of Synchrotron Radiation, 8, 314-316.

Rogers A.D. & Christensen P.R. (2007) Surface mineralogy of Martian low-albedo regions from MGS-TES data: Implications for upper crustal evolution and surface alteration. Journal of Geophysical Research, 112, E01003, doi:10.1029/2006JE002727.

Ruff S.W., Farmer J.D., Arvidson R.E., Squyres S.W. & Christensen P.R. (2008) The nature and distribution of silica at Home Plate in Gusev Crater, Mars: Evidence for a hydrothermal system. Lunar Planet Science Conf., Abstr. #2213.

Schwertmann, U., Friedl, J., and Kyek, A. (2004) Formation and properties of a continuous crystallinity series of synthetic ferrihydrites (2- to 6-line) and their relation to FeOOH forms. Clays and Clay Minerals, 52,221-226.

Singer R.B. (1982) Spectral evidence for the mineralogy of high-albedo soils and dust on Mars. Journal of Geophysical Research, 87, 10159-10168.

Squyres S.W., Arvidson R.E., Ruff S., Gellert R., Morris R.V., Ming D.W., Crumpler L., Farmer J.D., Des Marais D.J., Yen A., McLennan S.M., Calvin W., Bell J.F.I., Clark B.C., Wang A., McCoy T.J., Schmidt M.E. & de Souza P.A.J. (2008) Detection of Silica-Rich Deposits on Mars. Science, 320, 1063-1067, DOI: 10.1126/science.1155429.

Stöber W., Fink A. & Bohn E. (1968) Controlled growth of monodisperse silica spheres in the micron size range. Journal of Colloid and Interface Science, 26, 62-69.

Tsipursky, S.I. and Drits, V.A. (1984) The distribution of octahedral cations in the 2:1 layers of dioctahedral smectites studied by oblique-texture electron diffraction. Clay Minerals, 19,177-193.

Vaniman D.T., Bish D.L., Ming D.W., Bristow T.F., Morris R.V., Blake D.F., Chipera S.J., Morrison S.M., Treiman A.H., Rampe E.B., Rice M., Achilles C.N., Grotzinger J.P., McLennan S.M., Williams J., Bell J.F., Newsom H.E., Downs R.T., Maurice S., Sarrazin P., Yen A.S., Morookian J.M., Farmer J.D., Stack K., Milliken R.E., Ehlmann B.L., Sumner D.Y., Berger G., Crisp J.A., Hurowitz J.A., Anderson R., Des Marais D.J., Stolper E.M., Edgett K.S., Gupta S., Spanovich N. & Team M.S. (2014) Mineralogy of a Mudstone at Yellowknife Bay, Gale Crater, Mars. Science, 343, doi: 10.1126/science. 1243480.

Vantelon, D., Montarges-Pelletier, E., Michot, L.J., Pelletier, M., Thomas, F., and Briois, V. (2003) Iron distribution in the octahedral sheet of dioctahedral smectites. An Fe K-edge X-ray absorption spectroscopy study. Physics and Chemistry of Minerals, 30, 44-53.

Wells, N., Childs, C.W., and Downes, C.J., 1977, Silica Springs, Tongariro National Park, New Zealand-analyses of the spring water and characterisation of the alumino-silicate deposit: Geochimica et Cosmochimica Acta, v. 41, doi: 10.1016/0016-7037(77)90254-X.

Wyatt M.B. & McSween H.Y., Jr. (2002) Spectral evidence for weathered basalt as an alternative to andesite in the northern lowlands of Mars. Nature, 417, 263-266.

Yucelen, G.I., Choudhury, R.P., Vyalikh, A., Scheler, U., Beckham, H.W., and Nair, S. (2011) Formation of single- walled aluminosilicate nanotubes from molecular precursors and curved nanoscale intermediates. Journal of the American Chemical Society, 133, 5397-5412.